Numerical simulations of vapor kerosene/air rotating detonation engines with different slot inlet configurations

Fang Wang [a], Huangwei Zhang [b], Qiaodong Bai [a],[*], Chunsheng Weng [a]

[a] *National Key Laboratory of Transient Physics, Nanjing University of Science and Technology, Nanjing, 210094, China*
[b] *Department of Mechanical Engineering, National University of Singapore, Singapore, 117576, Singapore*

ARTICLE INFO

ABSTRACT

To investigate the effects of slot inlet configurations on premixed vapor kerosene/air rotating detonation engines, a series of cases with different injection patterns, including baseline inlet, outer slot inlet, middle slot inlet, and inner slot inlet, are simulated by solving three-dimensional reactive Euler equations. Stable rotating detonation waves were obtained in the baseline and the outer slot inlet cases. Instead, an unsteady triple-wave mode was obtained in the middle slot inlet case and a decoupled detonation was observed in the inner slot inlet case. A long supersonic injection zone was observed in the outer slot inlet case and the main total pressure loss was found in the buffer zone. The propagation mechanism analysis demonstrates the crucial role of the outer wall in the propagation of rotating detonation waves, where the detonation waves near the outer wall tend to be over-driven and contributes to the stable propagation of detonations. A positive mass average total pressure gain of 48.0% was obtained in the baseline, confirming the total pressure gain ability of the kerosene/air rotating detonation engines. The simulation results indicate the area ratio between the outlet and the inlet is of great importance for obtaining the positive total pressure gain.

1. Introduction

Rotating Detonation Engine (RDE) has attracted more and more attention over the past two decades because of its higher thermodynamic efficiency, continuous presence of detonation waves without multiple ignition, and compact engine geometry [1–3]. At present, most RDE research is based on hydrogen [4–9], and ethylene [10–13]. Relatively little attention has been given towards kerosene/air RDE. Due to space constraints and safety considerations, kerosene is deemed an ideal fuel for aviation engines [14,15]. Therefore, it is necessary to investigate kerosene/air RDE to achieve fundamental understandings for its potential applications, such as ramjet [16,17] and turbojet [18,19] engines.

Up to now, the successful initiation of kerosene/air rotating detonation in experiments remains challenging. For instance, Bykovskii et al. [20] investigated kerosene/air/oxygen rotating detonations and reported that rotating detonation waves can be obtained only by increasing the oxygen/nitrogen mass ratio to 1:1. Their subsequent research [21] focused on the addition of active fuels, e.g. hydrogen or syngas, to obtain the self-sustained rotating detonation waves with kerosene. MBDA France [22] conducted experiments on kerosene-fueled

RDE by heating the kerosene. The RDE combustor was connected to a ramjet test facility, which can provide up to 1 kg/s kerosene heated up to a maximum temperature of 800 K. Wu et al. [23] successfully obtained cracked kerosene/oxygen-enriched air rotating detonations with an oxygen mass fraction of 30%. Zheng et al. [24] investigated kerosene/oxygen-enrich air (35% oxygen) rotating detonations under a high total temperature (620K-860 K). From the foregoing literature, one may see that pre-vaporized kerosene can reduce the negative impacts from droplet breakup and evaporation [25–30] on the mixing and combustion. Hence vapor kerosene is expected in experiments to realize kerosene/air rotating detonation avoiding the addition of oxygen or hydrogen. The pre-vaporized process could be done by the hot wall of RDE or the high total temperature inflow or a precombustion chamber. Furthermore, a high injection total temperature can also promote the kerosene detonation and approach the practical operation condition for air-breathing engines.

Under high injection total temperature conditions, the inlet configuration should be deliberately designed to prevent the flashback, decrease the total pressure loss, and also maintain stable propagation of rotating detonation waves. Recently, Wu et al. [16] performed numerical research on H_2/air rotating detonation ramjet engine with a Laval

---

* Corresponding author.
  E-mail address: baiqd@njust.edu.cn (Q. Bai).

inlet. Two flow instabilities, i.e., backflow and strip-type fresh fuel layer, were analyzed while the potential effects of inlet configurations on RDE performance were not explored in their work. Wang et al. [31] numerically studied inlet area ratios on the performance of kerosene/air RDE by two-dimensional simulations. However, three-dimensional simulations are more relevant to practical problems such as the effects of inlet or chamber configurations. Betelin et al. [32] simulated the cylindrical RDE with an inner body extending out of the nozzle and thrust performance was analyzed. Bach et al. [33,34] experimentally investigated the total pressure gain performance of RDE. The total pressure gain performance was found to be a function of three variables, including injector area ratio, outlet area ratio, and combustor mass flux. Matsuoka et al. [35] measured the inlet blockage ratios on RDE with an axial outer slot inlet configuration. Their results imply that a reduction in the hydrodynamic blockage ratio while maintaining the geometric blockage ratio is required for stable RDE operation and total pressure gain. Zheng et al. [36,37] simulated the initiation process of a hydrogen/air RDE with three slot injection patterns. Their attention was paid to radial slot inlet configurations. While the axial slot inlet patterns that were commonly used in experiments [10,35,38] has not been investigated. With an axial slot inlet, the fresh mixture tends to accelerate to the supersonic conditions, which may cause uncertain consequences, e.g., reactant property change, total pressure loss, or even detonation failure. Also, the detonation propagation mechanism may vary a lot with different locations of the slot inlet. These potential effects play important roles in practical applications but are still not well understood now.

In this work, we aim to numerically investigate the premixed vapor kerosene/air RDE with different axial slot inlet configurations, including a baseline inlet, an outer slot inlet, a middle slot inlet, and an inner slot inlet. The rest of the paper is organized as below. In Section 2, the governing equation and physical model are presented. The numerical results are shown and discussed in Section 3. Finally, the main conclusions are summarized.

2. Governing equations and physical model

2.1. Governing equations

Three-dimensional Euler equations for multi-component reacting flows are solved, i.e.,

$$\frac{\partial \boldsymbol{U}}{\partial t} + \frac{\partial \boldsymbol{E}}{\partial x} + \frac{\partial \boldsymbol{F}}{\partial y} + \frac{\partial \boldsymbol{G}}{\partial z} = \boldsymbol{R} \tag{1}$$

where t, x, y, and z are time, x-, y- and z-direction coordinates, respectively. Y_i is the mass fraction of ith specie, ns is the number of species, ρ is the total mass density and calculated from $\rho = \sum_{i=1}^{ns} \rho Y_i$, u, v, and w are the velocity components in the x-, y- and z-directions, respectively, and p is the pressure. The total energy E is defined as

$$E = \rho h - p + \frac{\rho}{2}\left(u^2 + v^2 + w^2\right), \tag{3}$$

$$h = \sum_{i=1}^{ns} Y_i h_i, \tag{4}$$

where h_i is the enthalpy calculated by the thermochemical relation [39].

The production rate of ith specie due to chemical reactions, ω_i, is calculated by

$$\omega_i = W_i \sum_{k=1}^{nr} \left(v''_{ki} - v'_{ki}\right) RP_k, \tag{5}$$

where nr is the number of elementary reactions, v''_k and v'_k are the stoichiometric coefficients of reactants and products respectively, and RP_k is the reaction rate of the kth elementary reaction.

2.2. Numerical method and boundary conditions

In this study, an in-house three-dimensional Space-Time Conservation Element and Solution Element Method (CE/SE method) based on unstructured hexahedral meshes is employed to solve the governing equation. A κ-CNI scheme [31] is used to improve the shock capture abilities. The computing efficiency is improved by an MPI + OpenMP parallel strategy [40]. The source term is solved by a third-order total variation diminishing (TVD) Runge-Kutta method [41].

For the inlet boundary, an isentropic flow boundary condition [42, 43] is commonly used in RDE simulations. The local pressure and temperature at the head end are assumed as p_h and T_h. The injection total pressure and temperature are p_0 and T_0. The critical pressure is $p_{cr} = p_0\left(\frac{2}{\gamma+1}\right)^{\frac{\gamma}{\gamma-1}}$. The inlet boundary condition is divided into three cases:

When $p_h > p_0$, the slot inlet is treated as a solid wall and therefore it has

$$p = p_h, T = T_h, w = 0. \tag{6}$$

When $p_0 > p_h > p_{cr}$, the flows at the inlet are not choked and therefore it has

$$U = \begin{pmatrix} \rho Y_1 \\ \vdots \\ \rho Y_i \\ \vdots \\ \rho Y_{ns} \\ \rho u \\ \rho v \\ \rho w \\ E \end{pmatrix}, E = \begin{pmatrix} \rho Y_1 u \\ \vdots \\ \rho Y_i u \\ \vdots \\ \rho Y_{ns} u \\ \rho u^2 + p \\ \rho uv \\ \rho uw \\ (E+p)u \end{pmatrix}, F = \begin{pmatrix} \rho Y_1 v \\ \vdots \\ \rho Y_i v \\ \vdots \\ \rho Y_{ns} v \\ \rho vu \\ \rho v^2 + p \\ \rho vw \\ (E+p)v \end{pmatrix}, G = \begin{pmatrix} \rho Y_1 w \\ \vdots \\ \rho Y_i w \\ \vdots \\ \rho Y_{ns} w \\ \rho wu \\ \rho wv \\ \rho w^2 + p \\ (E+p)w \end{pmatrix}, R = \begin{pmatrix} \omega_1 \\ \vdots \\ \omega_i \\ \vdots \\ \omega_{ns} \\ 0 \\ 0 \\ 0 \\ 0 \end{pmatrix}, \tag{2}$$

$$p = p_h, T = T_0 \left(\frac{p_h}{p_0}\right)^{\frac{\gamma}{\gamma-1}}, w = \sqrt{\frac{2\gamma}{\gamma-1} R T_0 \left[1 - \left(\frac{p_h}{p_0}\right)^{\frac{\gamma-1}{\gamma}}\right]}. \tag{7}$$

When $p_{cr} > p_h$, the flows at the inlet are choked and therefore it has

$$p = p_{cr}, T = T_0 \left(\frac{p_{cr}}{p_0}\right)^{\frac{\gamma}{\gamma-1}}, w = \sqrt{\frac{2\gamma}{\gamma-1} R T_0 \left[1 - \left(\frac{p_{cr}}{p_0}\right)^{\frac{\gamma-1}{\gamma}}\right]}. \tag{8}$$

Besides, a non-reflective boundary [43] based on local Mach number is employed on the outlet. A slip wall boundary condition is developed and adopted in chamber walls. These boundary conditions are commonly used in RDE simulations.

2.3. Chemical reaction mechanism and validations

A two-step kerosene/air chemical reaction mechanism [44] is employed in this paper. The kerosene is referred as KERO and it is a linear combination of $C_{10}H_{22}$, C_9H_{12}, C_9H_{18}. The chemical reaction mode contains six species (KERO, O_2, CO, CO_2, H_2O, N_2) and is composed of two reactions corresponding to the fuel oxidation into CO and H_2O, and CO–CO_2 equilibrium. The two reactions are

$$\frac{KERO + O_2 \Rightarrow CO + H_2O}{CO + O_2 \Leftrightarrow CO_2}, \tag{9}$$

where the forward reaction rates are written as

$$\frac{k_{f1} = A_1 f_1(\varphi) e^{(-E_{a,1}/RT)} [KERO]^{n_{KERO}} [O_2]^{n_{O_2,1}}}{k_{f2} = A_2 f_2(\varphi) e^{(-E_{a,2}/RT)} [CO]^{n_{CO}} [O_2]^{n_{O_2,2}}}. \tag{10}$$

The coefficients of the two reaction rates are shown in Table 1 [44]. It should be noted that $f_1(\varphi)$ and $f_2(\varphi)$ corresponding to equivalence ratio φ are correction functions to adjust the flame speed, which can be found in Ref. [44].

The numerical method and chemical reaction model have been validated with one-dimension detonation waves in our previous work [31,40]. Since the one-dimensional detonation speed of the two-step chemistry has been well validated with Jet-A fuel within an equivalence ratio of 0.8–1.4 in our previous work [40], here we continue validating the two-step kerosene/air chemistry from theoretical prediction with a detailed mechanism JetSurf 2.0 [45]. A theoretical prediction tool SDToolbox [46] is employed to compute the ZND structures with the two mechanisms. The detonation properties between the two-step chemistry and detailed chemistry at $p = 1$ MPa and $T = 800$ K are shown in Fig. 1(a)-(c). This condition is close to that in the fresh mixture layer of the RDE in this work. It can be found that the differences are generally small. For example, the difference in the von Neumann pressure is less than 3%. Fig. 1(d) shows the ignition delay time validation with experiments of Zhukov at al. [47], Dagaut et al. [48], Zhang et al. [49], and Dean et al. [50] with stoichiometric KERO/air mixture at initial pressure 10 atm. The result indicates the ignition delay time agrees well with the experiments. These results demonstrate that the two-step chemistry is reasonable for kerosene/air detonation simulations. Besides, it is worth noting that this two-step chemistry has also been validated with experimental detonation speed by Ren et al. [51] and successfully applied in oblique detonation simulations [52].

2.4. Physical model and grid independence

The model RDE is a 3D annular combustor with different inlet configurations, i.e., baseline (Fig. 2(a)), outer slot inlet (Fig. 2(b)), middle slot inlet (Fig. 2(c)), and inner slot inlet (Fig. 2(d)). In these configurations, the outer and inner diameters of the RDE chambers are 72 mm and 60 mm, respectively, which corresponds to a chamber width of 6 mm. Meanwhile, the axial length is 60 mm. As shown in Fig. 2(a), in the baseline case, the inlet width is equal to the chamber width. Fig. 2(b), (c), and 2(d) show the schematic of the outer slot inlet, middle slot inlet, and inner slot inlet, respectively. The slot inlet widths in these cases remain the same, i.e., 2 mm, which corresponds to one-third of the inlet width in the baseline. This slot width is close to that used in the RDE experiments [10,35,38]. Two probes installed on the inner and outer wall of the head end, i.e., $P_{innerwall}$ and $P_{outerwall}$, are used to monitor detonation waves in the four cases.

To investigate the effects of inlet configurations, the injection condition keeps the same for the four cases. Specifically, the premixed stoichiometric kerosene/air mixture is injected from the inlet into the chamber with a total pressure of 20 atm and a total temperature of 800 K. This total pressure promotes a stable rotating detonation wave [40, 53]. The total temperature is favorable to have full evaporation of the liquid kerosene and is in the reasonable range for an inflow heater in experiments [24,54].

The grid independence has been analyzed by one-dimensional detonations with different grid sizes, i.e., 0.1, 0.2, and 0.3 mm in our previous work [31,40]. Similar detonation velocity is obtained by the above grids. Reasonable results of the grid independence and C-J detonation velocity can be obtained with a grid of 0.2 mm. Hence the grid sizes used in the present paper are between 0.15 and 0.2 mm.

Moreover, the computational domain is discretized with three resolutions, i.e., $29 \times 220 \times 960$ cells (coarse), $39 \times 260 \times 1200$ cells (medium), and $49 \times 310 \times 1500$ cells (fine), respectively. Note that the z-direction grids (i.e., RDE height direction) are stretched with ensuring that the grids near the head end are sufficiently fine. The simulation condition remains the same for the three meshes, i.e., at $p_0 = 20$ atm, $T_0 = 800$ K, and $\varphi = 1$ with the baseline inlet model. Table 2 shows the computed detonation wave speed and height with the foregoing meshes, whilst Fig. 3 compares the overall flow structure from the three meshes at the same instant ($t = 0.83$ ms) when the detonation wave has propagated over seven cycles. In general, the results from the above meshes are fairly close, which confirms that the flow structures are not sensitive to the mesh resolutions. Therefore, the medium mesh is used in the following analysis based on the acceptable computational cost and accuracy.

3. Results and discussion

3.1. The flow field in the baseline case

Fig. 4 shows the internal flow field structure of the baseline case. It can be seen that a single-wave detonation wave propagates circumferentially in the chamber. Upstream of the detonation wave, a triangular fresh mixture layer is formed and bounded by the burned gas with an interface called deflagration surface. Downstream of the detonation wave, an oblique shock wave can be observed and followed by a slip line. The detonation front, deflagration surface, and oblique shock wave constitute a typical triple point structure in the chamber. Several reflected shock waves appear near the inlet surface behind the detonation front. With decreased pressure close to the head end, the fresh mixture begins to be injected behind the reflected shock waves. High-speed burned gas is exhausted from the outlet and thus generates thrust. These typical flow structures are similar to the 3D simulation results of Katta [55] and experimental observations of Rankin [38] and Anand [56], proving the rationality of our numerical simulations.

Fig. 5 shows the detailed temperature, pressure, and numerical

Table 1
Reaction rate coefficients(mol,s,cm³,K,cal).

	KERO oxidation	CO–CO₂ equilibrium
Activation energy	4.15×10^4	2.0×10^4
Pre-exponential factor	8.00×10^{11}	4.5×10^{10}
Reaction exponents	n_{KERO} 0.55	n_{CO} 1.00
	$n_{O_2,1}$ 0.90	$n_{O_2,2}$ 0.50
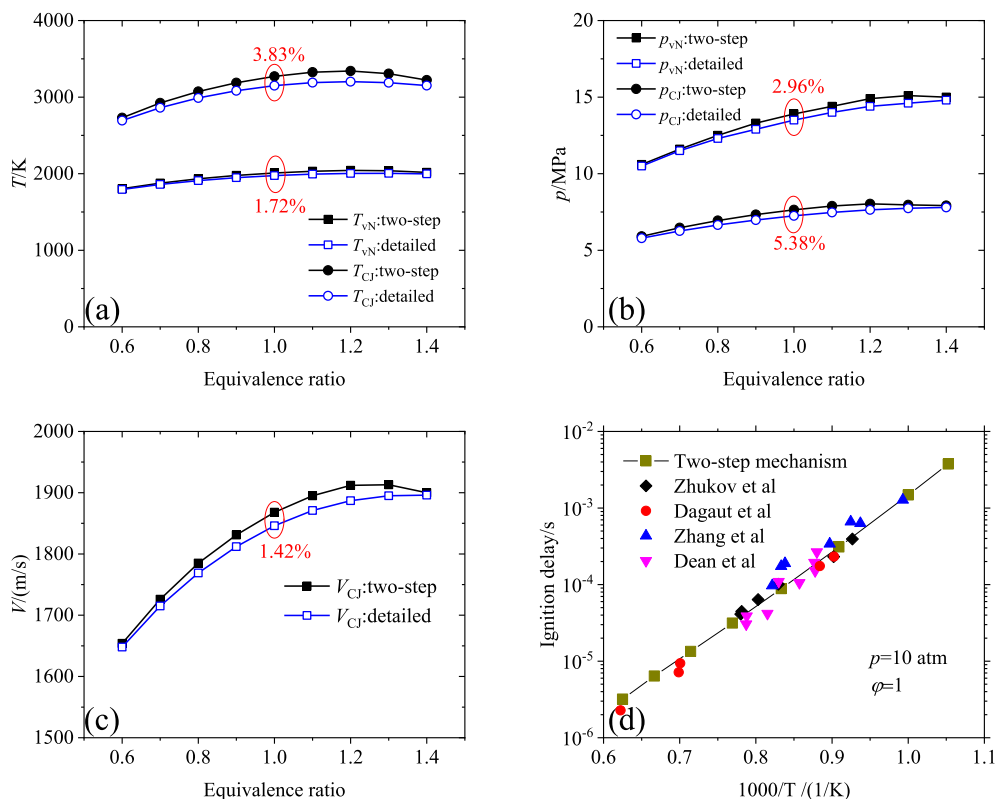
Fig. 1. (a)–(c): comparison of von Neumann (vN) and Chapman–Jouguet (C–J) properties between the two-step and detailed chemical mechanisms, (d): comparison of ignition delay time with experiments using stoichiometric KERO/air mixture at initial pressure 10 atm.
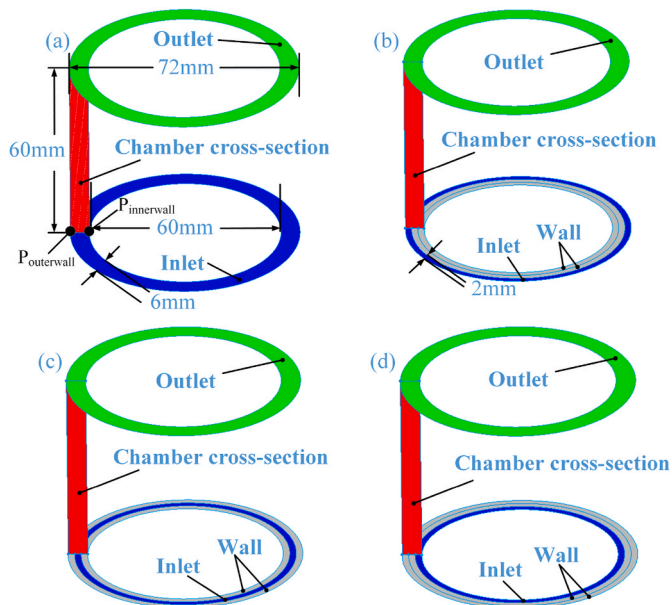
Fig. 2. Schematic of 3D RDE physical models: (a) baseline inlet, (b) outer slot inlet, (c) middle slot inlet, and (d) inner slot inlet.

Table 2
Mesh resolution effects on RDE operation performance.

Mesh	Total cell number	Detonation height/mm	Detonation speed/(m/s)
Coarse	6,124,800	27.2	1762.4
Medium	12,168,000	27.4	1771.3
Fine	22,785,000	27.5	1775.8

schlieren ($|\nabla\rho|$) contours in the baseline case. The detonation wave has propagated over ten cycles and become fully developed. The flow field structure is observed to remain the same at different times, and the detonation wave is steady because of the ideal injection condition. As shown in Fig. 5, the peak pressure couples closely with the peak temperature, indicating the typical characteristics of detonation waves. Due to the convergence effects of the outer wall, the thickness of the detonation front on the outer wall is much larger than that of the inner wall. The difference in detonation strength on the inner and outer walls results in the appearance of the reflected shock waves downstream of the detonation front [55]. These reflected shock waves start from the inlet surface and extend to the detonation product downstream of the detonation front, generating the secondary shock waves under the slip line. As shown in Fig. 5(d), the first reflected shock wave (I-RSW1) is very strong, which nearly approaches the detonation front on the inner wall.

Fig. 6 shows the pressure and temperature histories recorded by two probes located at the head end. As can be seen, after several cycles, the fluctuations in pressure and temperature peaks are small, indicating that a stable operation of RDE is achieved. As shown in Fig. 6, the peak pressure on the outer wall is approximately 14 MPa while it only reaches 11 MPa on the inner wall. The peak temperature on the outer wall is also higher than that on the inner wall. This indicates the detonation strength near the outer wall is much higher than that near the inner wall. The calculated propagation frequency is 8547 Hz, which corresponds to an average detonation speed of 1771.3 m/s computed by the average radius of the inlet surface. The theoretical C-J detonation speed calculated with the parameters in the fresh mixture layer is 1856 m/s. Therefore, the mean detonation speed is $0.95V_{C\text{-}J}$. It is worth noting that the detonation speed on the outer wall is $1.04V_{C\text{-}J}$, which corroborates that the detonation wave on the outer wall is slightly over-driven. However, the detonation speed is only $0.87V_{C\text{-}J}$ on the inner wall.

From the enlarged view (Fig. 6b and d), several pressure and temperature jumps can be found behind the detonation front, which is
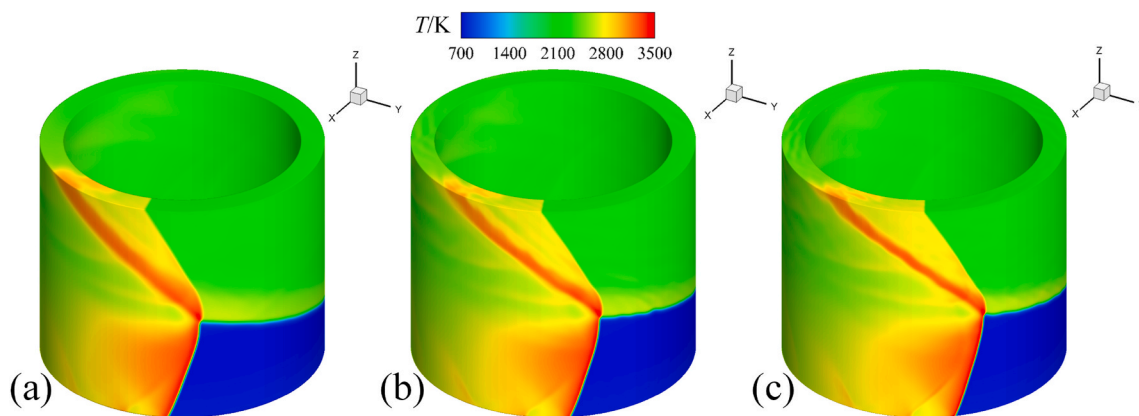
Fig. 3. Comparison of temperature contours from (a) coarse, (b) medium, and (c) fine meshes.
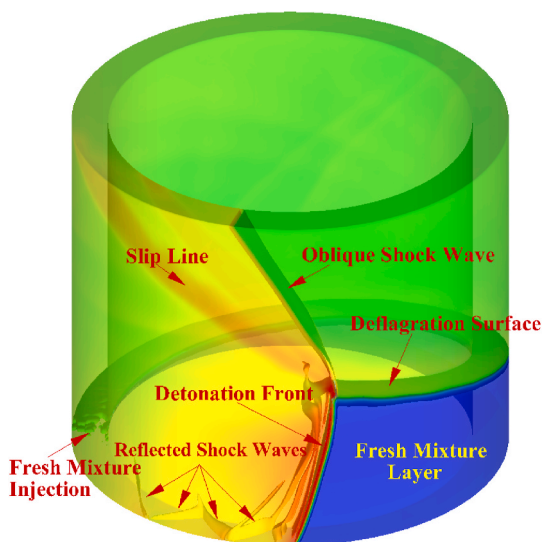
Fig. 4. Internal flow field structure in the baseline case.

caused by the reflected shock waves behind the detonation front. These reflected shock wave signals agree well with the experimental signals obtained by Wolański [57]. As can be seen, fuel injection is delayed due to the high pressures of the reflected shock waves. The pressure of the first reflected shock wave on the inner wall (I-RSW1) reaches 7.37 MPa. It decreases to 5.34 MPa for I-RSW2 and 3.61 MPa for I-RSW3. For the reflected shock waves on the outer wall, relatively lower pressure peaks are obtained, such as 6.2 MPa for O-RSW1, 4.6 MPa for O-RSW2, and 2.6 MPa for O-RSW3. These reflected shock waves are responsible for the high-pressure region on the inlet surface blocking the fresh mixture injection. The fuel injection time occupies about 70% of the detonation propagation time in one cycle. Decreasing the pressure of these reflected shock waves can significantly increase the fuel injection occupation and decrease the flashback problem.

3.2. The flow field in the slot inlet cases

A slot inlet configuration is commonly used to accelerate the fresh mixture and prevent flashback problems. The propagation mode and the flow field structure with such configurations may differ from those in the baseline case. In this section, the rotating detonation flow field with different slot inlet configurations, including outer slot inlet, middle slot inlet, and inner slot inlet, are analyzed.
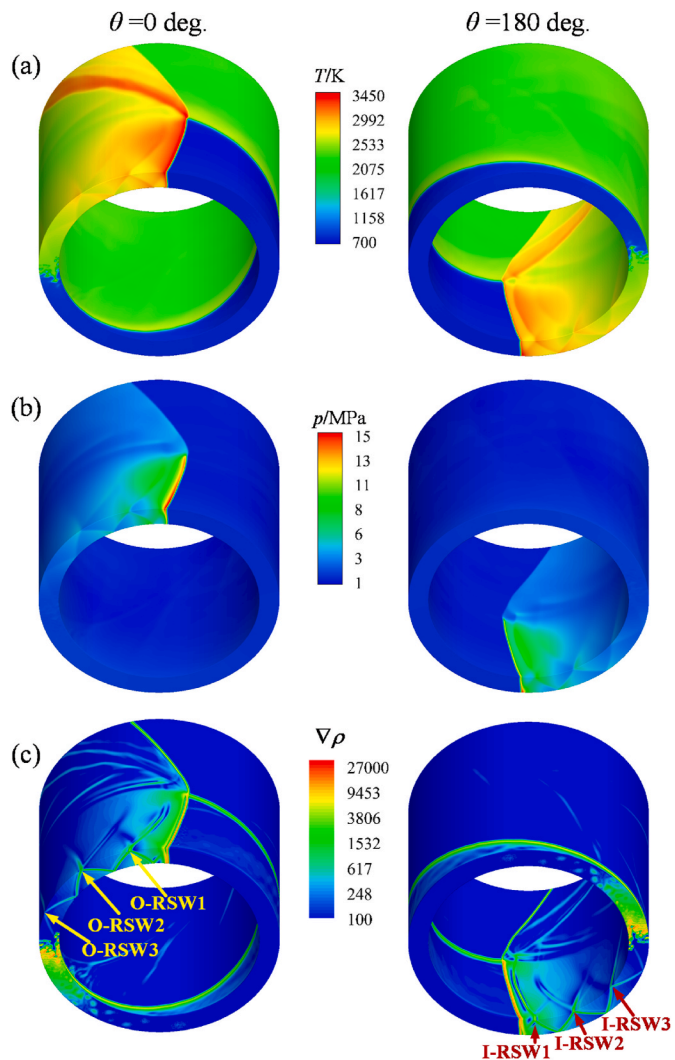
Fig. 5. Contours in the baseline case: (a) pressure, (b) temperature, (c) numerical schlieren ($|\nabla\rho|$). O-RSW1, O-RSW2, O-RSW3: the first, second, third reflected shock wave on the outer wall. I-RSW1, I-RSW2, I-RSW3: the first, second, third reflected shock wave on the inner wall.

3.2.1. Outer slot inlet

Fig. 7 shows the internal flow field structure of RDE with an outer slot inlet. It is drawn with an iso-surface of density gradient magnitude overlaid with the temperature. To display the overall internal flow
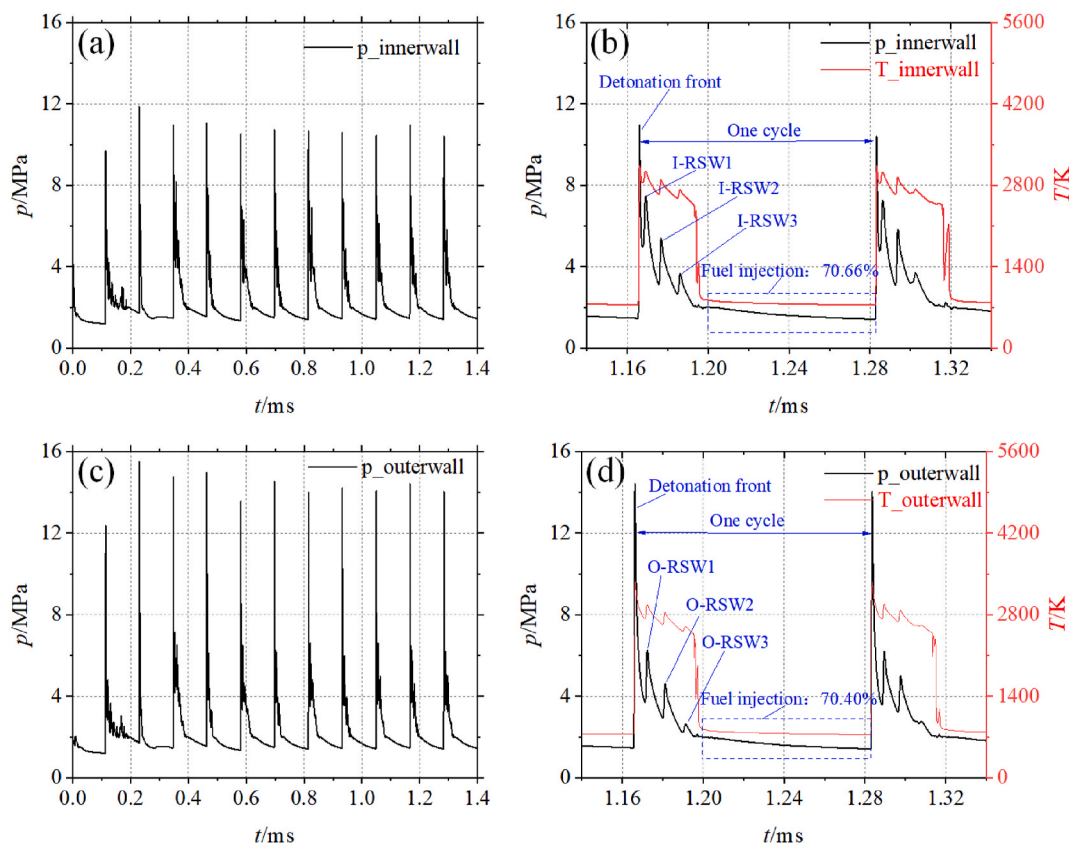
Fig. 6. Time history of (a) pressure on the outer wall, (b) enlarged view of pressure and temperature on the outer wall, (c) pressure on the inner wall, and (d) enlarged view of pressure and temperature on the inner wall in the baseline case.
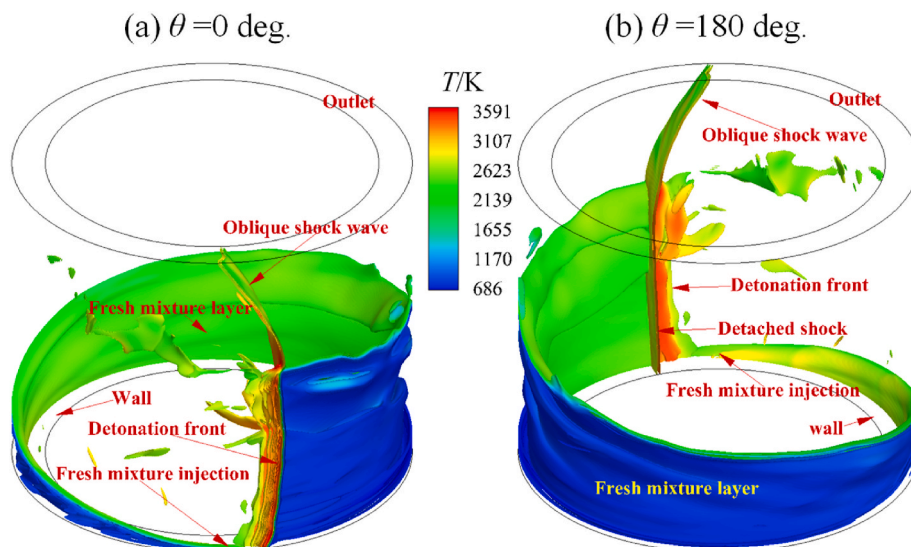
Fig. 7. Internal flow field structure in the outer slot inlet case. The iso-surface (geometry) is numerical schlieren ($|\nabla\rho|$) between 800 and 25,000 and the surface contour is temperature.

structure, two views with $\theta = 0°$ and $\theta = 180°$ are presented. As can be seen, a single-wave stable detonation wave is obtained in this case. However, different features appear in this case. As shown in Fig. 7(b), a detached shock appears in the burned gas, which travels ahead of the detonation front. Although the detonation waves only exist near the outer wall, the leading shock of the detonation front still extends to the inner wall and a full-scale oblique shock is formed.

Fig. 8 shows the detailed temperature, pressure, and numerical schlieren contours in the outer slot inlet case. The height of the detonation wave is about 35 mm. The peak pressure and temperature reach 15 MPa and 3591 K. The area blocked by the detonation front on the inlet is decreased compared with the baseline, which promotes the injection of the mixture. The reflected shock waves are not observed downstream of the detonation waves. The location of the fresh mixture injection closely follows the detonation front, indicating that the outer slot inlet can significantly increase the fresh mixture injection
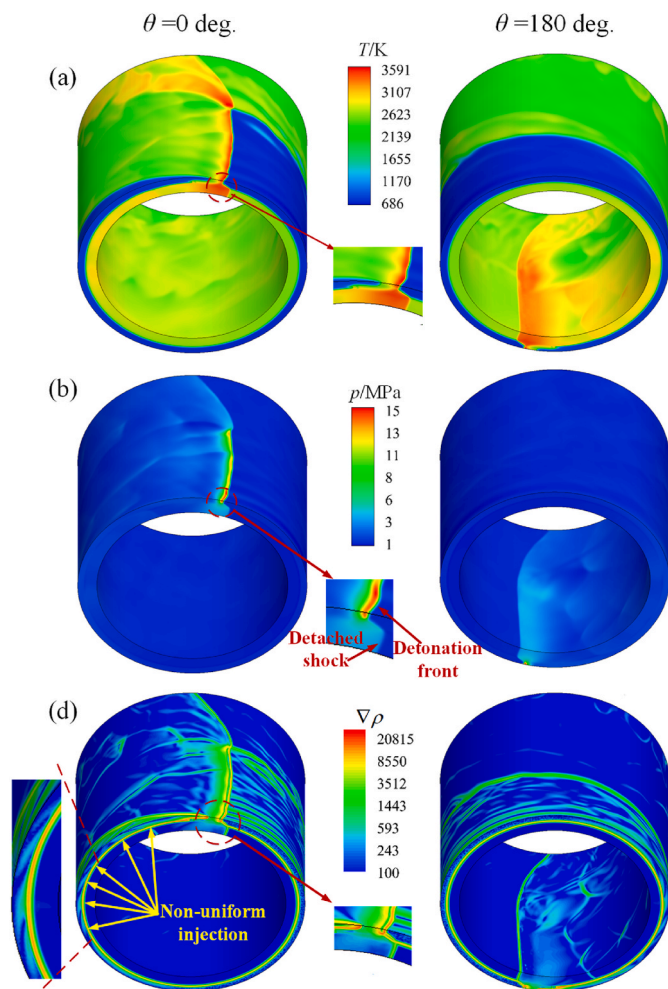
Fig. 8. Contours in the outer slot inlet case: (a) pressure, (b) temperature, (c) numerical schlieren.

occupation with maintaining the stable propagation of rotating detonation waves. It is found that the fresh mixture shows a non-uniform distribution on the inlet surface, which is not observed in the baseline case. As can be seen, the fresh mixture near the outer wall injects earlier because the detonation product has a lateral expansion effect towards the inner wall. Therefore, the pressure decreases fast and the injection begins earlier near the outer wall. The non-uniform injection is thus formed. Overall, the slot inlet leads to lots of unsteady phenomena and obtains a more complex flow field structure.

Fig. 9 shows the pressure and temperature histories recorded by the two probes. It can be found that the detonation waves propagate stably for over ten cycles. The pressure peak on the outer wall reaches around 13 MPa. For the probe located on the inner wall, only detached shocks are recorded, whose pressure peak is approximately 3.5 MPa. Fig. 9 also validates the continuous existence of the typical flow structure in the outer slot inlet case. The pressure peaks and temperature peaks are coupled closely. These features confirm the continued existence of a steady detonation wave in this case. From Fig. 9(b), it is found that the fuel injection time occupation reaches about 98%. Comparing the baseline with the outer slot inlet case, one can see that with decreased inlet area, the fuel injection occupation in one cycle increases, and the hydrodynamic blockage ratio decreases. This trend agrees well with the experiments by Matsuoka et al. [35]. These results indicate that an outer slot inlet can realize self-sustained rotating detonation waves and obtain a low hydrodynamic blockage ratio.

The calculated average propagation frequency is 8811 Hz. The average detonation speed is 1937 m/s using the middle radius of the outer slot inlet surface, which corresponds to $1.04V_{C-J}$. The calculated detonation speed is $1.07V_{C-J}$ on the outer wall and $1.01V_{C-J}$ for the inner diameter of the outer slot inlet surface. Therefore, it can be found the detonation is fully over-driven in the outer slot inlet case.

3.2.2. Middle slot inlet

Fig. 10 shows the internal flow structure in the middle slot inlet case. Fig. 10(a) is an iso-surface of density gradient magnitude overlaid with the temperature. Similarly, Fig. 10(b) shows the Mass fraction of kerosene (MF kerosene) distribution overlaid with heat release rate(HRR). As can be seen, the main flow field structure includes the detonation waves, fresh mixture layer, unburned pockets, oblique shock waves, and deflagration surface. The fresh mixture layer shows a T-shaped structure, which agrees with the observation in the study by Zheng et al. [36, 37]. Three counter-clockwise propagating detonation waves are observed, namely DW1, DW2, and DW3. Upstream of the DW1, a fresh mixture layer is formed, and the deflagration surface can be found on the interface between the fresh mixture layer and burned product.

It is worth noting that there is some fresh mixture remaining existing downstream of DW1 due to the weakness of the detonation waves. The most intense heat release happens near the triple point, on top of which there is still some fresh mixture. As a result, the fresh mixture on top of the triple point is isolated from the major fresh mixture layer and becomes unburned pockets. These unburned pockets are engulfed into the expansion product and release heat far away from the leading shock. Furthermore, as shown in Fig. 10(b), the unburned pockets are burned with a considerable heat release rate in the expansion process, which tends to generate compression waves and thus form a reverse blast wave propagating towards the next shock wave.

Fig. 11 shows the contours of temperature, pressure, heat release rate (HRR), and numerical schlieren in the middle inlet slot case. It can be found the flow field is complex due to the weak detonation waves and the reverse blast waves(RBWs). The peak pressure and temperature of the detonation waves are 5.2 MPa and 3069 K, which are far below the values in the baseline case. The fresh mixture can be injected from almost the whole slot inlet. An obvious RBW is observed downstream of the DW3. From the HRR and numerical schlieren contours, it can be found that several compressive waves and a considerable heat release rate can be seen from the triple point of DW3 to the RBW. This phenomenon implies the generation mechanism of the reverse blast waves. These RBWs travel in the reverse direction of the shock waves and bring much disturbance and complexity to the internal flow field.

Fig. 12 shows the pressure and temperature histories recorded by two probes. The propagation mode is unsteady. The enlarged views (Fig. 12(b) and d) present the pressure and temperature of the three detonation waves in two cycles. As can be seen, three unsteady detonation waves namely DW1, DW2, and DW3 propagate periodically. The pressure peaks of the shock waves are relatively low and may split into several sub-peaks due to the influence of the RBW. This phenomenon is more like the instability propagation mode measured by experiments [24]. The calculated average propagation frequency is 5353 Hz. The average propagating speed is about 1109 m/s, which corresponds to $0.60V_{C-J}$.

3.2.3. Inner slot inlet

In this section, the RDE with an inner slot inlet is simulated. Fig. 13 shows the pressure and temperature histories recorded by the two probes. It can be found that the detonation wave is extinguished after six cycles. The result indicates that the rotating detonation waves cannot propagate continuously with an inner slot inlet. The pressure peak of the detonation wave is around 10 MPa before it is decoupled. The pressure history on the outer wall also indicates there is a detached shock coupled with the detonation wave.

Fig. 14 shows the pressure and temperature contours at $t = 0.62$ ms and $t = 1.22$ ms. As can be seen, the detonation wave has not been
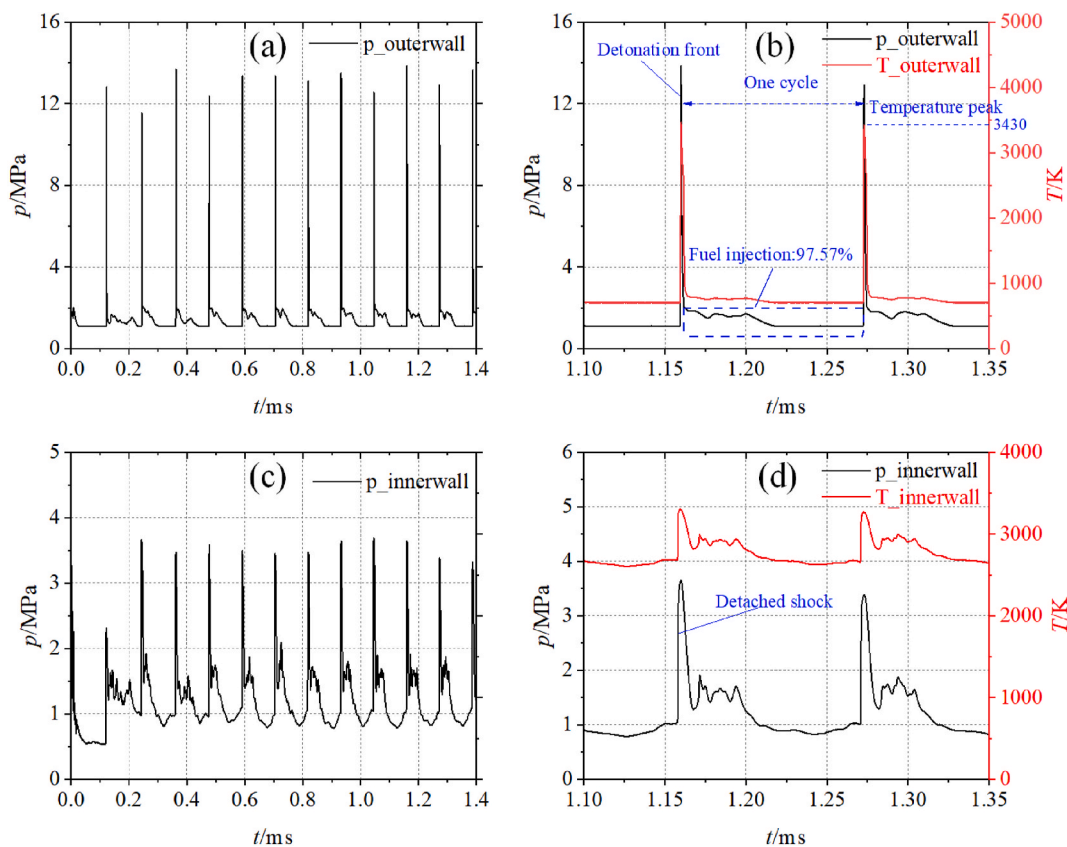
Fig. 9. Time history of (a)pressure on the outer wall, (b)enlarged view of pressure and temperature on the outer wall, (c)pressure on the inner wall, and (d)enlarged view of pressure and temperature on the inner wall in the outer slot inlet case.
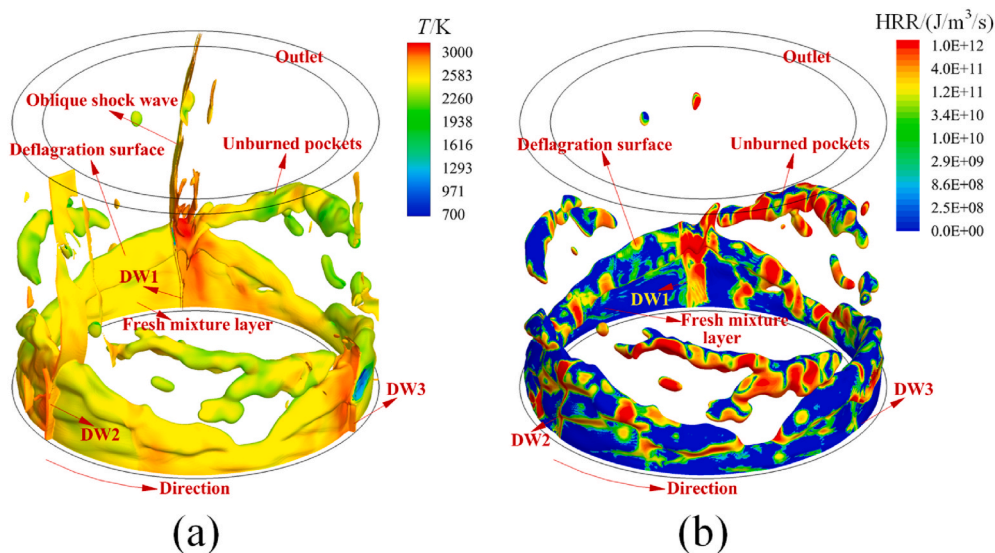
Fig. 10. Internal flow field structure in the middle slot inlet case. (a) Iso-surface(geometry) is numerical schlieren ($|\nabla\rho|$) between 500 and 20000. Surface contour is temperature; (b) Iso-surface (geometry) is the mass fraction of kerosene between 0 and 0.062. Surface contour is the heat release rate(HRR).

decoupled at 0.62 ms. However, it can be found that the unburned zone begins to appear near the upper end of the detonation waves. The appearance of the unburned cold mixture along the slip line would affect the generation of new transverse waves and thus quench the detonation waves [15]. As shown in Fig. 14(b), the detonation wave has decoupled $t = 1.22$ ms, and the fresh mixture is injected from the whole inlet. The frequency of the detonation wave before failure is 7589 Hz. The mean

propagating speed is 1477 m/s calculated by the average diameter of the inner slot. The detonation speed only reaches $0.8V_{C\text{-}J}$.

3.3. Reactant properties in the fresh mixture layer

The inlet configurations are of great importance because it not only determines the stable propagation of rotating detonation waves but also
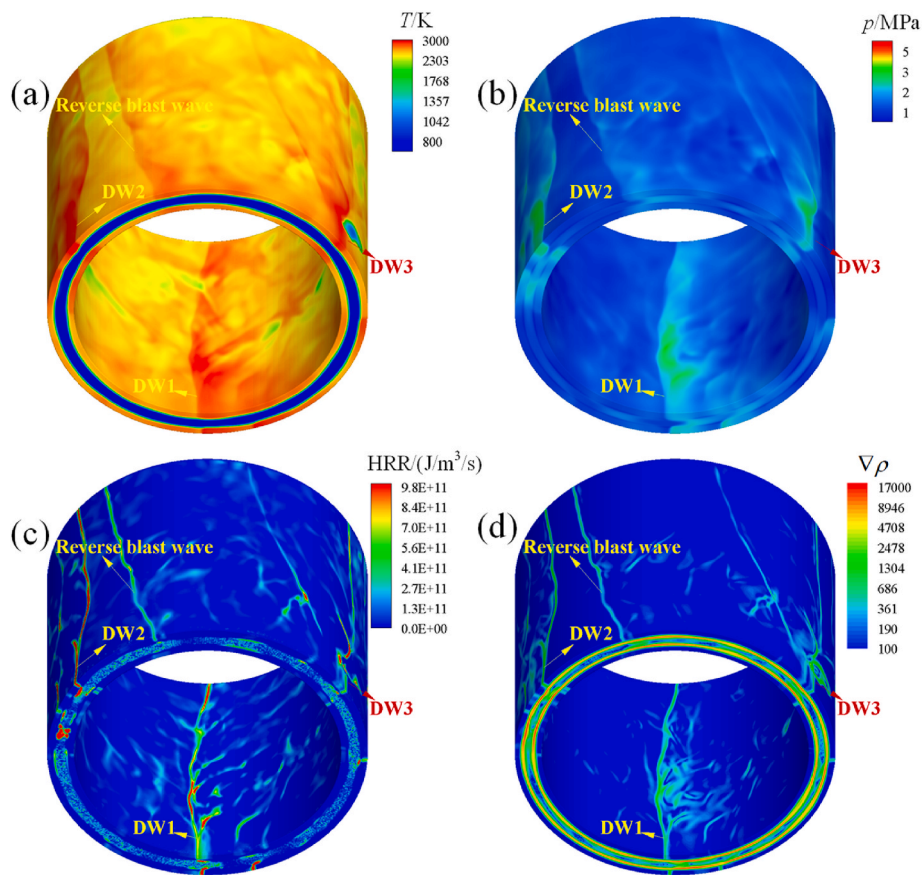
Fig. 11. Contours in the middle slot inlet case: (a) temperature, (b) pressure, (c) HRR, and (d) numerical schlieren ($|\nabla\rho|$).

directly affects the reactant properties and structures of the fresh mixture layer [36,37]. The reactant properties, such as the density, mass fraction of fuel, and temperature, would also influence the detonation strength in turn. Besides, a slot inlet configuration is always accompanied with supersonic injection and shock waves. As a result, total pressure loss is unavoidable. Investigations of the reactant properties can provide insights into the detailed evolution of flow dynamics and provide useful information for the practical RDE design.

As we know, the height of the fresh mixture layer is largest immediately before the detonation front. Hence, the reactant properties in the fresh mixture layer before the detonation front can be used to predict the final status of the reactants. Fig. 15(a)-(d) show the slice contours of MF kerosene, total pressure, Mach number, and temperature in the fresh mixture layer before the detonation front in the baseline case. The fresh mixture is injected with a subsonic speed and accelerates in the fresh mixture layer. The total pressure is uniformly distributed in the fresh mixture layer. Fig. 15(e) shows the distributions of total pressure, temperature, Mach number, and density along the extracted line (middle radius) in Fig. 15(a). As can be seen, the Mach number increases and the density decreases first, which means the fresh mixture undergoes acceleration when injected into the chamber. During this process, the total pressure and static temperature show a slight decrease because the fresh mixture does work while expanding. After that, the Mach number and density tend to be constant. The maximum total pressure loss reaches approximately 5%. Due to the interaction of the fresh mixture and burned gas, the total pressure near the interface decreases fast.

Fig. 16 shows the reactant properties in the fresh mixture layer before the detonation front in the outer slot inlet case. As we can see, due to the channel expansion in the outer slot inlet, the fresh mixture is injected with sonic speed and then accelerated to supersonic condition when entering the combustor chamber. The injection blows away the

burned gas and forms a fresh mixture layer near the outer wall. As shown in Fig. 16(d), the total pressure in the fresh mixture layer can maintain about 2 MPa, except for the buffer zone. The total pressure in the buffer zone drops fast due to the interaction between the burned gas and fresh mixture jet flow. As shown in Fig. 16(e), due to the gas expansion, the fresh mixture is injected supersonically. Negligible total pressure loss is observed in the supersonic injection zone. The maximum total pressure loss was observed in the buffer zone, which is approximately 20%. As can be seen, the fresh mixture expands and does work in the buffer zone, which mainly accounts for the total pressure loss. It is worth noting that the fresh mixture injection has reached a choking condition while it only has a Mach number of 0.74 in the baseline.

For the middle inlet slot case, an unsteady triple-wave mode is formed. Fig. 17 shows the reactant properties in the fresh mixture layer before the DW3. As can be seen, the fresh mixture is surrounded by burned gas. Deflagration tends to occur on the interface of the fresh mixture and burned gas, which thus influences the fresh mixture layer. The height of the fresh mixture layer is around 0.02 m, which is relatively lower. Fig. 17(e) shows the parameters along the extracted line in Fig. 17(a). The total pressure decreases fast when the fresh mixture is injected, which reaches approximately 18%. It is observed that the density of the fresh mixture shows a similar tendency with the total pressure, which implies the decrease of total pressure may mainly result from the fresh mixture expansion. Besides, the fresh mixture expands to the two sides, which enhances the deflagration.

3.4. Propagation mechanism of rotating detonation waves

The simulation results indicate the inlet configurations significantly affect the RDE operation mode. In this section, the propagation mechanism of the rotating detonation wave in different inlet configurations
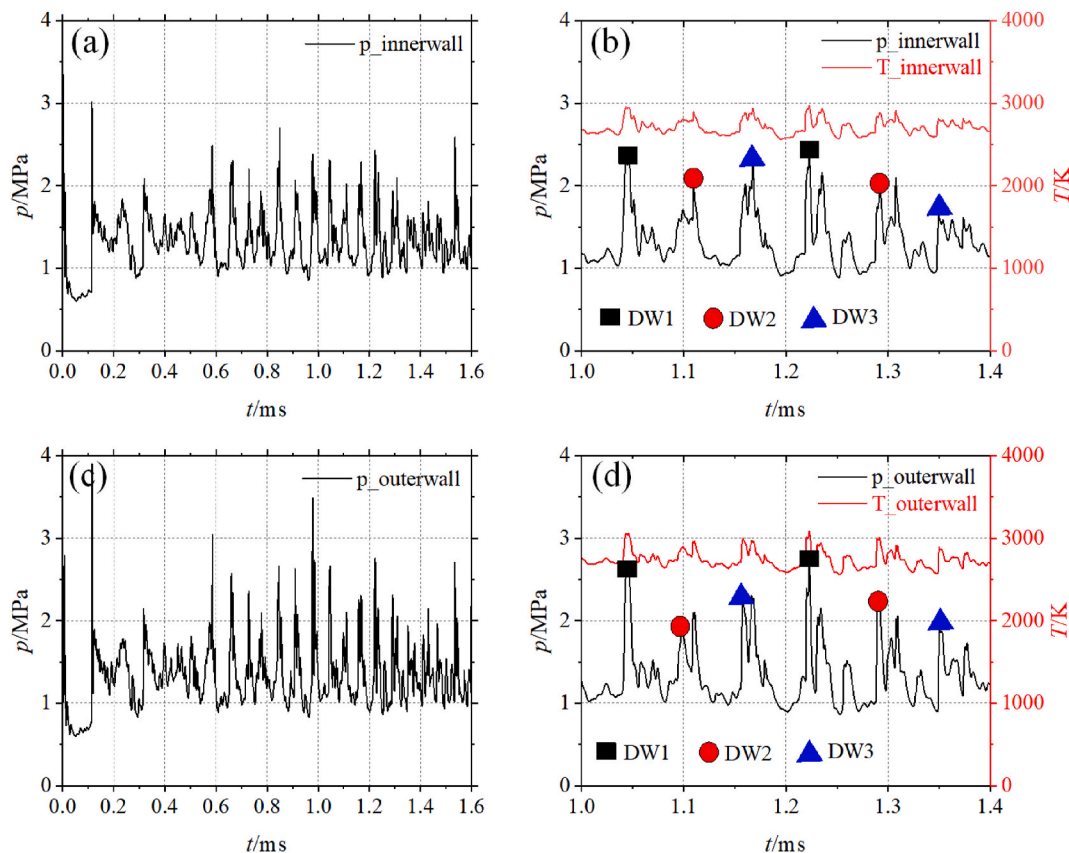
Fig. 12. Time history of (a) pressure on the outer wall, (b) enlarged view of pressure and temperature on the outer wall, (c) pressure on the inner wall, and (d) enlarged view of pressure and temperature on the inner wall in the middle slot inlet case.
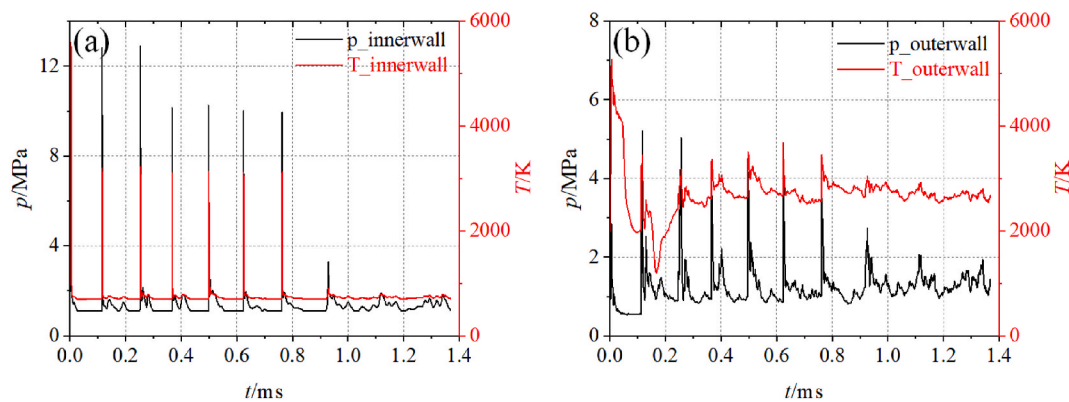
Fig. 13. Time history of (a) pressure and temperature on the outer wall, and (b) pressure and temperature on the inner wall in the inner slot inlet case.

will be analyzed. Figs. 18–21 show the temperature, pressure, and numerical schlieren contours on the head end in the four cases.

As shown in Fig. 18, the detonation front is slightly inclined in the baseline case. The detonation front on the inner wall moves ahead of that on the outer wall due to the expansion effect of the inner wall and the compression effect of the outer wall [55]. The compression effect of the outer wall enhances the detonation near the outer wall and thus forms the over-driven Mach detonation [58]. The Mach detonation is followed by a reactive reacting zone with strong heat release. Moreover, there is also an oblique shock wave connected with the Mach stem, which propagates towards the inner wall.

As shown in Fig. 19, the wave structure in the outer slot case consists of a strong Mach detonation wave propagating along the outer wall, a detached shock propagating in the burned gas, and a transmitted shock

wave connecting the detonation wave and detached shock wave. Such a shock structure is similar to the layered detonation problems [59], where detonations propagate through a layer of reactant that is bounded by an inert gas. The reason accounting for the appearance of the leading detached shock and the transmitted oblique shock is the low acoustic impedance between the burned gas and reactant. As discussed by Houim [59], the detached shocks can contribute to the generation of new triple points that are necessary to the propagation of detonation waves. However, a low acoustic impedance can lead to the insufficient generation of triple points and thus cause detonation failure. In this 3D case, strong confinement is provided by the outer wall. Due to the convergence effects of the outer wall, the detonation near the outer wall is developed to be an over-driven Mach detonation [58,60]. Therefore, despite of the low acoustic impedance of 0.51 between burned gas and
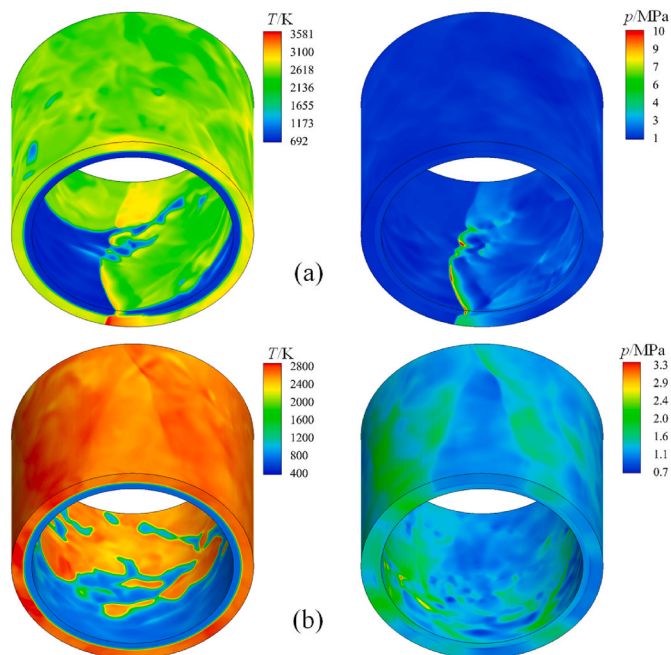
Fig. 14. Temperature and pressure contours in the inner slot inlet case. (a) t = 0.62 ms (Detonation has not decoupled). (b) t = 1.22 ms (Detonation is extinguished).

reactant, the rotating detonation wave can still stably propagate. This result demonstrates the crucial role of the outer wall in the RDE design. Moreover, the rotating detonation can also appear in a hollow combustor [61–63]. That is to say, such a detonation structure can be self-sustained. Most of the detonation product expands to the inner wall direction, leading to an increase in the pressure and temperature in the burned gas.

As shown in Fig. 20, the three detonation waves and the reverse blast

waves can be captured in the middle slot inlet case. It can be found that the shock wave near the outer wall is stronger than that on the inner wall. However, there is no reactant near the outer wall. Hence the shock waves are lacking in enough support of the reacting zone. As a result, the detonation strength is very weak. The incomplete coupling of the leading shock and reaction zone brings disturbances and instabilities, such as the reverse combustion waves, to the downstream flow.

Fig. 21 shows the flow field contours in the inner slot case at $t = 0.62$ ms when the detonation wave still exists. The typical structure is similar to the one in the outer slot inlet case. The difference is that the two sides of the detonation wave exhibit poor confinement, which cannot support the stable propagation of detonation waves. Compared with the outer slot inlet, the main detonation region in this case is near the inner wall. However, on the inner side, the inner wall provides an expansion effect for the propagation of detonation waves. On the outer side, the burned gas works as a weak confinement, which is also insufficient to reflect or generate enough transverse waves. The acoustic impedance ratio is approximate 0.51. Such a low acoustic impedance ratio exhibits poor confinement compared with the solid wall. The situation gets worse especially when the detonation propagates along a circular channel in which strong confinement is needed from the outer side to continuously change the detonation direction.

3.5. RDE operation performance analysis

To explore the operation performance of vapor kerosene/air RDE, the mass flow averaged outlet total pressure $p_{total,outlet}$, total temperature $T_{total,outlet}$, outlet Mach number Ma_{outlet}, and outlet mean flow angle α_{outlet} are calculated according to [64].

$$\zeta_{outlet} = \frac{\int_{outlet} \rho w \zeta dA}{\int_{outlet} \rho w dA} \tag{11}$$

Note that the mass flow averaged value is a surface integral performed on the outlet surface.

Mass flow averaged total pressure gain is computed by
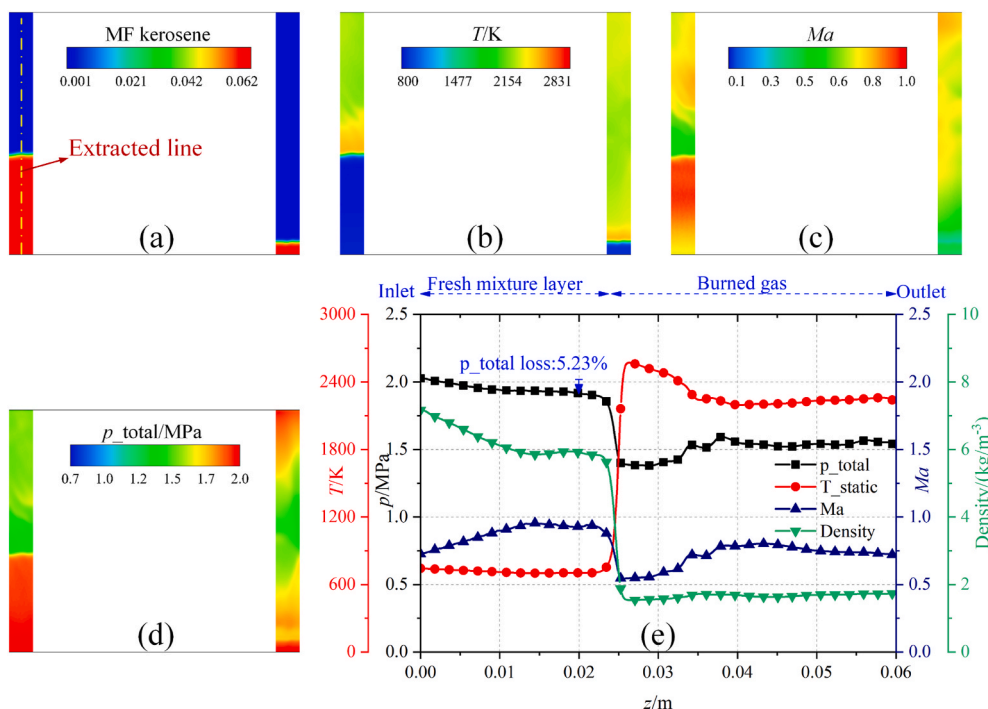
Fig. 15. Reactant properties in the baseline case: (a) kerosene mass fraction, (b) temperature, (c) Mach number, (d) total pressure. (e) Total pressure, temperature, Mach number, and density distributions along the dashed line in (a).
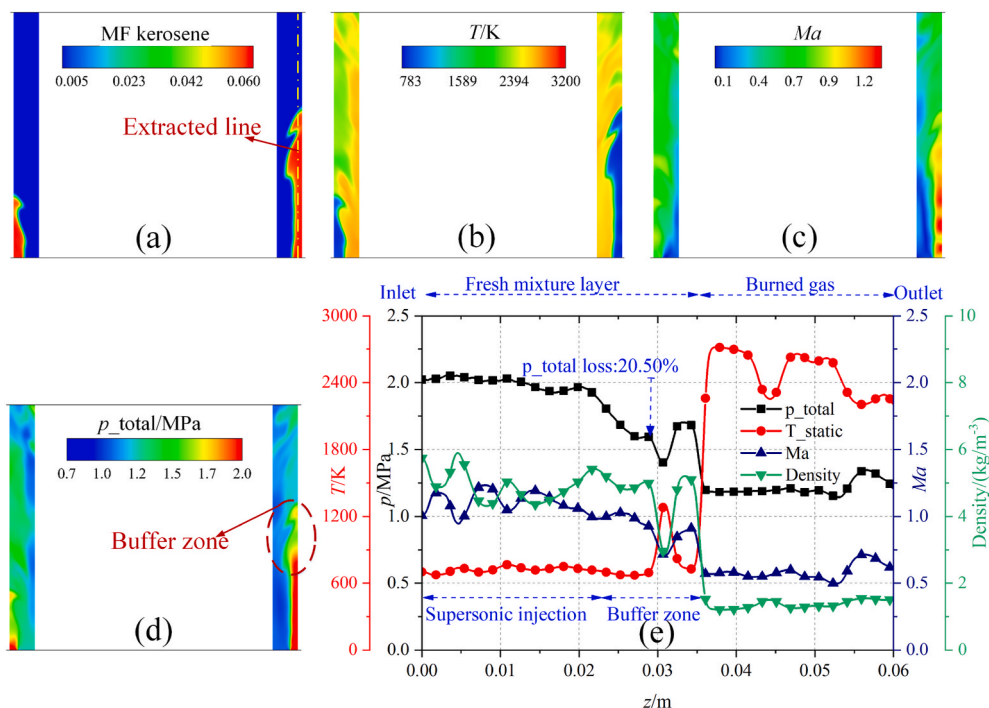
Fig. 16. Reactant properties in the outer slot inlet case: (a) kerosene mass fraction, (b) temperature, (c) Mach number, (d) total pressure. (e) Total pressure, temperature, Mach number, and density distributions along the dashed line in (a).
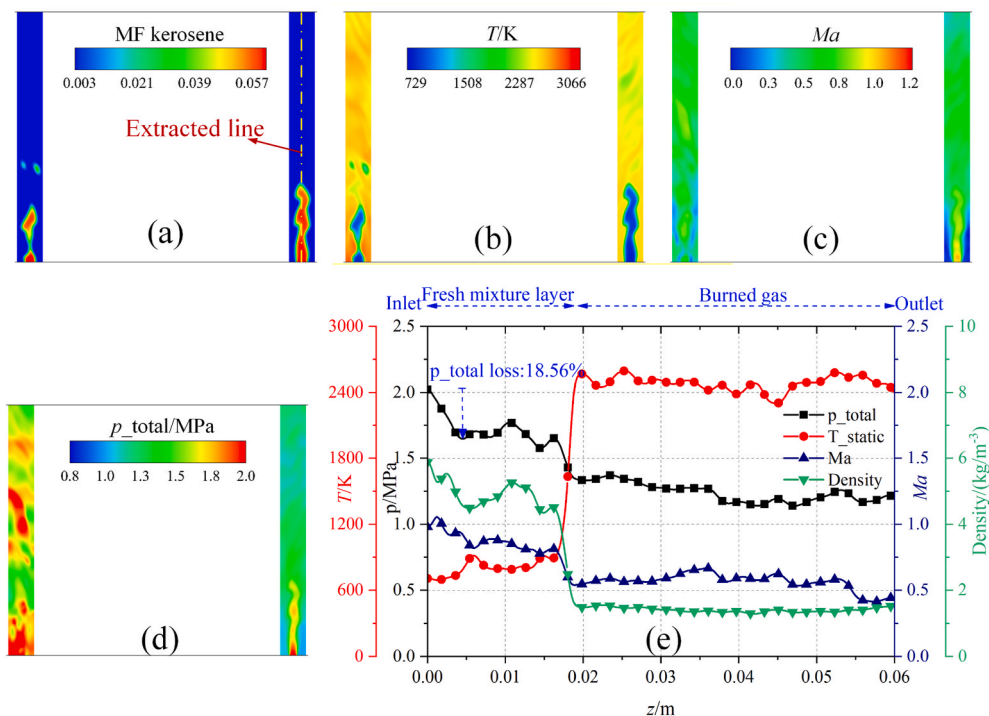
Fig. 17. Reactant properties in the middle slot inlet case: (a) kerosene mass fraction, (b) temperature contour, (c) Mach number, (d) total pressure, and (e) total pressure, temperature, Mach number, and density distribution along the dashed line in (a).

$$p_{\text{total,gain}} = \frac{p_{\text{total,outlet}} - p_{\text{total,inlet}}}{p_{\text{total,inlet}}}. \tag{12}$$

Table 3 shows the RDE performance of the four simulated cases. For the total pressure gain performance, a positive pressure gain of 48.0% is obtained in the baseline. It is an inspiring result that proves the pressure gain ability of a vapor kerosene/air RDE. As predicted by Braun [64],

mass flow averaged total pressure gain of a H_2/Air RDE can reach 130% in their baseline case without nozzles. The present simulation result is in a reasonable range because the reactivity of kerosene is significantly lower than H_2. In the outer slot inlet case, the total pressure gain ability decreases to −19.1%. Since the total pressure gain is computed by the mass flow averaged method, it can be found that the differences mainly
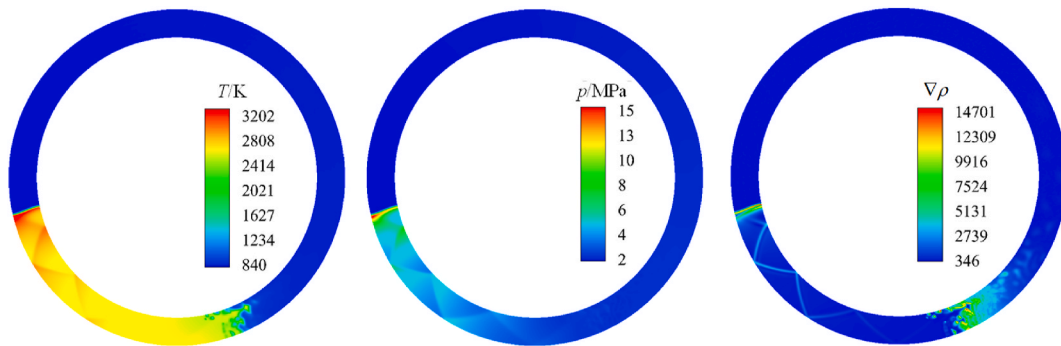
Fig. 18. Temperature, pressure, and numerical schlieren contours in the baseline case.
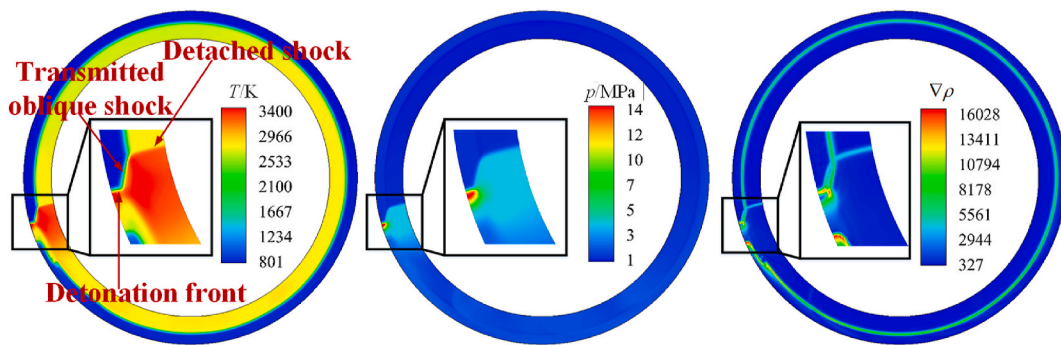
Fig. 19. Temperature, pressure, and numerical schlieren contours in the outer slot inlet case.
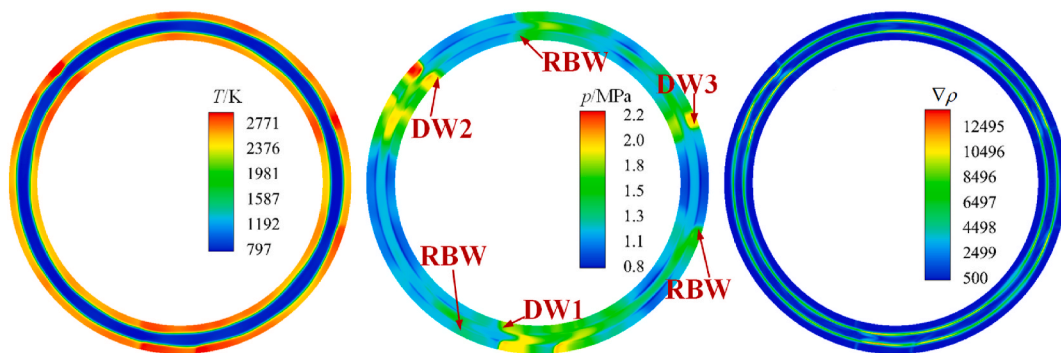
Fig. 20. Temperature, pressure, and numerical schlieren contours in the middle slot inlet case.
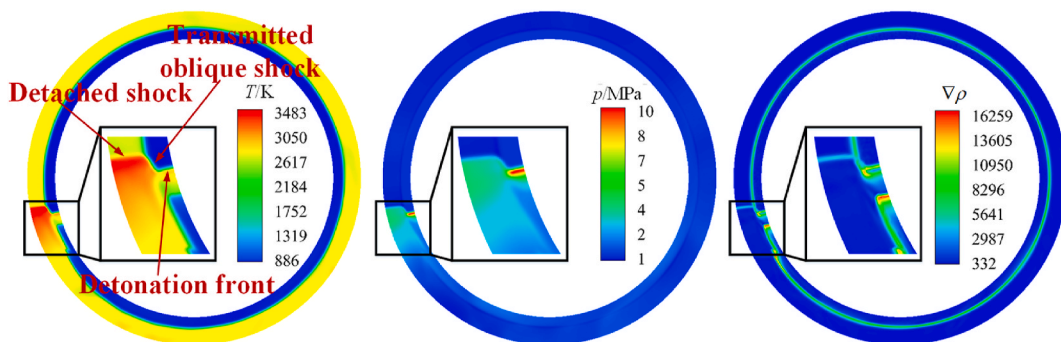
Fig. 21. Temperature, pressure, and numerical schlieren contours in the inner slot inlet case at t = 0.62 ms (before detonation failure).

Table 3
RDE operation performance.

	Baseline	Outer slot inlet	Middle slot inlet	Inner slot inlet
Propagation Mode	Single-wave	Single-wave	Triple-wave	Decoupled
Frequency/Hz	8547	8811	5353	–
V/(m/s)	1771.3	1936.7	1109.8	–
V/V_{CJ}	0.95	1.04	0.60	–
$p_{total,\ gain}$	48.0%	−19.1%	−27.5%	–
$T_{total,\ outlet}$/K	2684.1	2585.9	2614.6	–
Ma_{outlet}	0.87	0.66	0.58	–
α_{outlet}/degree	71.7	70.3	81.0	–

result from the use of slot inlet. Due to the use of slots, the inlet area decreases while the outlet area remains the same. Hence the ratio of outlet area/inlet area significantly increases. The injection flow expands and does work in the combustion chamber, which causes total pressure loss and leads to the negative total pressure gain. Therefore, the positive total pressure gain is expected to be obtained, for example, by decreasing the outlet throat area or increasing the injection area. The critical area ratio between the outlet and the inlet for obtaining the positive total pressure gain and maintaining the stable detonation is of great importance. It is also worth noting that the total pressure gain shows a notable decrease in the unsteady triple-wave mode compared with the stable single-wave detonation case. Such a result indicates that it is necessary to ensure the stable propagation of the detonation waves and reduce the reverse blast waves to improve self-pressurization ability of RDE.

The total temperature can be used to indicate the energy that can be extracted from the outlet. As can be seen, the total temperature remains high without the nozzle. The Mach number in the baseline is 0.87, while it decreases to 0.66 in the outer slot inlet. These results also predict decreasing the inlet area would cause lots of drawbacks such as a lower outlet Mach number and a lower total pressure gain. Besides, the flow angle in detonation cases is significantly lower than that in deflagration cases, predicting that there is much more circumferential velocity component in the detonation cases. Therefore, fully utilizing the momentum in the RDE outlet would be a key factor to improve the propulsive performance.

4. Conclusion

In this paper, the effects of various slot inlet configurations on the premixed vapor kerosene/air RDE were numerically studied. A two-step kerosene/air chemistry was adopted and the stoichiometric kerosene/air mixture was injected. The detonation structure, reactant properties, propagation mechanism, and the operation performance were analyzed. The main conclusions are summarized as follows.

A stable single-wave rotating detonation was obtained in the baseline and the outer slot inlet case. An unsteady triple-wave mode was obtained in the middle slot inlet and a decoupled detonation was observed in the inner slot inlet case. In baseline, the injection speed of the fresh mixture is subsonic with a total pressure loss of 5.2% and a fresh mixture injection occupation of 70.4%. For the outer slot inlet, supersonic injection of the fresh mixture was observed. There is a relatively low total pressure loss in the supersonic injection stage and the fresh mixture injection occupation reaches 97.6%, which predicts the optimal inlet configuration design. The total pressure loss is 18.6% in the middle slot inlet and the fresh mixture was injected almost on the whole inlet surface.

The outer wall plays a crucial role in the self-sustained propagation of rotating detonation waves. Due to the compression effect of the outer wall, the detonation near the outer wall tends to be over-driven and thus forms a Mach detonation. The burned gas and the inner wall exhibit poor confinement and cannot support the stable propagation of rotating

detonation waves. A positive total pressure gain of 48.0% is obtained in the baseline, which confirms the total pressure gain ability of kerosene/air RDE. However, a negative total pressure gain is obtained in the slot inlet cases. The simulation results indicate the critical area ratio between the outlet and the inlet is of great importance for obtaining the positive total pressure gain.

Declaration of competing interest

The authors declare that they have no known competing financial interests or personal relationships that could have appeared to influence the work reported in this paper.

Acknowledgment

References

[1] J.Z. Ma, M.-Y. Luan, Z.-J. Xia, J.-P. Wang, S.-j. Zhang, S.-b. Yao, B. Wang, Recent progress, development trends, and consideration of continuous detonation engines, AIAA J. 58 (2020) 4976–5035.

[2] K. Kailasanath, Recent developments in the research on pressure-gain combustion devices, in: Innovations in Sustainable Energy and Cleaner Environment, 2020, pp. 3–21.

[3] P. Wolanski, Detonative propulsion, Proc. Combust. Inst. 34 (2013) 125–158.

[4] Z. Xia, H. Ma, G. Ge, C. Zhou, Effects of ignition condition on the initiation characteristics of rotating detonation wave in plane-radial structure, Acta Astronaut. 175 (2020) 79–89.

[5] C. Yan, H. Teng, H.D. Ng, Effects of slot injection on detonation wavelet characteristics in a rotating detonation engine, Acta Astronaut. 182 (2021) 274–285.

[6] J. Sun, J. Zhou, S. Liu, Z. Lin, Numerical investigation of a rotating detonation engine under premixed/non-premixed conditions, Acta Astronaut. 152 (2018) 630–638.

[7] J. Sun, J. Zhou, S. Liu, Z. Lin, Interaction between rotating detonation wave propagation and reactant mixing, Acta Astronaut. 164 (2019) 197–203.

[8] J. Sun, J. Zhou, S. Liu, Z. Lin, J. Cai, Effects of injection nozzle exit width on rotating detonation engine, Acta Astronaut. 140 (2017) 388–401.

[9] J. Sun, J. Zhou, S. Liu, Z. Lin, W. Lin, Effects of air injection throat width on a non-premixed rotating detonation engine, Acta Astronaut. 159 (2019) 189–198.

[10] S. Zhou, H. Ma, C. Zhou, N. Hu, Experimental research on the propagation process of rotating detonation wave with a gaseous hydrocarbon mixture fuel, Acta Astronaut. 179 (2021) 1–10.

[11] Y. Wang, J. Le, A rotating detonation engine using methane-ethylene mixture and air, Acta Astronaut. 188 (2021) 25–35.

[12] N.N. Smirnov, V.B. Betelin, V.F. Nikitin, Y.G. Phylippov, J. Koo, Detonation engine fed by acetylene–oxygen mixture, Acta Astronaut. 104 (2014) 134–146.

[13] G. Wang, W. Liu, S. Liu, H. Zhang, H. Peng, Y. Zhou, Experimental verification of cylindrical air-breathing continuous rotating detonation engine fueled by non-premixed ethylene, Acta Astronaut. (2021).

[14] F.L. Song, Y. Wu, S.D. Xu, X.K. Yang, X. Chen, The impact of fuel ratio and refueling mode on pre-combustion cracking properties of RP-3 kerosene, Int. J. Hydrogen Energy 45 (2020) 28505–28519.

[15] A.K. Hayashi, N. Tsuboi, E. Dzieminska, Numerical study on JP-10/air detonation and rotating detonation engine, AIAA J. 58 (2020) 5078–5094.

[16] K. Wu, S.J. Zhang, M.Y. Luan, J.P. Wang, Effects of flow-field structures on the stability of rotating detonation ramjet engine, Acta Astronaut. 168 (2020) 174–181.

[17] N.N. Smirnov, V.F. Nikitin, L.I. Stamov, E.V. Mikhalchenko, V.V. Tyurenkova, Rotating detonation in a ramjet engine three-dimensional modeling, Aero. Sci. Technol. 81 (2018) 213–224.

[18] P. Wolański, Application of the continuous rotating detonation to gas turbine, Appl. Mech. Mater. 782 (2015) 3–12.

[19] Y.W. Wu, C.S. Weng, Q. Zheng, W.L. Wei, Q.D. Bai, Experimental research on the performance of a rotating detonation combustor with a turbine guide vane, Energy 218 (2021).

[20] F.A. Bykovskii, S.A. Zhdan, E.F. Vedernikov, Continuous spin detonation of fuel-air mixtures, Combust. Explos. Shock Waves 42 (2006) 463–471.

[21] F.A. Bykovskii, S.A. Zhdan, E.F. Vedernikov, Continuous detonation of the liquid kerosene—air mixture with addition of hydrogen or syngas, Combust. Explos. Shock Waves 55 (2019) 589–598.

[22] B. Le Naour, F.H. Falempin, K. Coulon, MBDA R&T effort regarding continuous detonation wave engine for propulsion - status, 2016, in: 21st AIAA International Space Planes and Hypersonics Technologies Conference, Xiamen, China, 2017.

[23] Y. Zhong, Y. Wu, D. Jin, X. Chen, X. Yang, S. Wang, Effect of channel and oxidizer injection slot width on the rotating detonation fueled by pre-combustion cracked kerosene, Acta Astronaut. 165 (2019) 365–372.

[24] Q. Zheng, H.L. Meng, C.S. Weng, Y.W. Wu, W.K. Feng, M.L. Wu, Experimental research on the instability propagation characteristics of liquid kerosene rotating detonation wave, Def. Technol. 16 (2020) 1106–1115.

[25] N.N. Smirnov, V.B. Betelin, A.G. Kushnirenko, V.F. Nikitin, V.R. Dushin, V. A. Nerchenko, Ignition of fuel sprays by shock wave mathematical modeling and numerical simulation, Acta Astronaut. 87 (2013) 14–29.

[26] V.B. Betelin, N.N. Smirnov, V.F. Nikitin, V.R. Dushin, A.G. Kushnirenko, V. A. Nerchenko, Evaporation and ignition of droplets in combustion chambers modeling and simulation, Acta Astronaut. 70 (2012) 23–35.

[27] N.N. Smirnov, A.B. Kiselev, A.I. Nazarenko, V.V. Tyurenkova, I.V. Usovik, Physical and mathematical models for space objects breakup and fragmentation in hypervelocity collisions, Acta Astronaut. 176 (2020) 598–608.

[28] N.N. Smirnov, K.A. Kondratyev, Evaluation of craters formation in hypervelocity impact of debris particles on solid structures, Acta Astronaut. 65 (2009) 1796–1803.

[29] N.N. Smirnov, V.F. Nikitin, V.R. Dushin, Y.G. Filippov, V.A. Nerchenko, J. Khadem, Combustion onset in non-uniform dispersed mixtures, Acta Astronaut. 115 (2015) 94–101.

[30] V.V. Tyurenkova, N.N. Smirnov, V.M. Guendugov, Analytical solution for a single droplet diffusion combustion problem accounting for several chain reaction stages, Acta Astronaut. 83 (2013) 208–215.

[31] F. Wang, C.S. Weng, Y.W. Wu, Q.D. Bai, Q.A. Zheng, H. Xu, Numerical research on kerosene/air rotating detonation engines under different injection total temperatures, Aero. Sci. Technol. 103 (2020).

[32] V.B. Betelin, V.F. Nikitin, E.V. Mikhalchenko, 3D numerical modeling of a cylindrical RDE with an inner body extending out of the nozzle, Acta Astronaut. 176 (2020) 628–646.

[33] E. Bach, P. Stathopoulos, C.O. Paschereit, M.D. Bohon, Performance analysis of a rotating detonation combustor based on stagnation pressure measurements, Combust. Flame 217 (2020) 21–36.

[34] E. Bach, C.O. Paschereit, P. Stathopoulos, M.D. Bohon, An empirical model for stagnation pressure gain in rotating detonation combustors, Proc. Combust. Inst. 38 (2021) 3807–3814.

[35] K. Matsuoka, M. Tanaka, T. Noda, A. Kawasaki, J. Kasahara, Experimental investigation on a rotating detonation cycle with burned gas backflow, Combust. Flame 225 (2021) 13–19.

[36] Y.S. Zheng, C. Wang, Y.H. Wang, Y. Liu, Z.H. Yan, Numerical research of rotating detonation initiation processes with different injection patterns, Int. J. Hydrogen Energy 44 (2019) 15536–15552.

[37] Y.S. Zheng, C. Wang, B.G. Xiao, Y. Liu, J.H. Cai, Numerical simulation of radial-stratified rotating detonation flow field structures with different injection patterns, Int. J. Hydrogen Energy 45 (2020) 32619–32631.

[38] B.A. Rankin, D.R. Richardson, A.W. Caswell, A.G. Naples, J.L. Hoke, F.R. Schauer, Chemiluminescence imaging of an optically accessible non-premixed rotating detonation engine, Combust. Flame 176 (2017) 12–22.

[39] A. Burcat, B. Ruscic, Chemistry, third millennium ideal gas and condensed phase thermochemical database for combustion with updates from active thermochemical tables, J. Chem. Inf. Model. (2005).

[40] F. Wang, C.S. Weng, Y.W. Wu, Q.D. Bai, Q. Zheng, H. Xu, Effects of total pressures and equivalence ratios on kerosene/air rotating detonation engines using a paralleling CE/SE method, Def. Technol. 17 (2021) 1805–1816.

[41] G.-S. Jiang, C.-W. Shu, Efficient implementation of weighted ENO schemes, J. Comput. Phys. 126 (1996) 202–228.

[42] M.J. Zhao, H.W. Zhang, Origin and Chaotic Propagation of Multiple Rotating Detonation Waves in Hydrogen/air Mixtures, 2020, p. 275. Fuel.

[43] Z.-d. Lei, Z.-w. Chen, X.-q. Yang, J. Ding, P.-f. Weng, Operational mode transition in a rotating detonation engine, J. Zhejiang Univ. - Sci. 21 (2020) 721–733.

[44] B. Franzelli, E. Riber, M. Sanjosé, T. Poinsot, A two-step chemical scheme for kerosene–air premixed flames, Combust. Flame 157 (2010) 1364–1373.

[45] H. Wang, E. Dames, B. Sirjean, D.A. Sheen, A High-Temperature Chemical Kinetic Model of N-Alkane (Up to N-Dodecane), Cyclohexane, and Methyl-, Ethyl-, N-Propyl and N-Butyl-Cyclohexane Oxidation at High Temperatures, 2010 in, 19 September.

[46] J.Z.S. Browne, J.E. Shepherd, Numerical Solution Methods for Shock and Detonation Jump Conditions, 2018.

[47] V.P. Zhukov, V.A. Sechenov, A.Y. Starikovskiy, Autoignition of kerosene (Jet-A)/air mixtures behind reflected shock waves, Fuel 126 (2014) 169–176.

[48] P. Dagaut, M. Cathonnet, The ignition, oxidation, and combustion of kerosene: a review of experimental and kinetic modeling, Prog. Energy Combust. Sci. 32 (2006) 48–92.

[49] C. Zhang, B. Li, F. Rao, P. Li, X. Li, A shock tube study of the autoignition characteristics of RP-3 jet fuel, Proc. Combust. Inst. 35 (2015) 3151–3158.

[50] A.J. Dean, O.G. Penyazkov, K.L. Sevruk, B. Varatharajan, Autoignition of surrogate fuels at elevated temperatures and pressures, Proc. Combust. Inst. 31 (2007) 2481–2488.

[51] Z.X. Ren, B. Wang, Numerical study on stabilization of wedge-induced oblique detonation waves in premixing kerosene-air mixtures, Aero. Sci. Technol. 107 (2020).

[52] Z. Ren, B. Wang, G. Xiang, L. Zheng, Numerical analysis of wedge-induced oblique detonations in two-phase kerosene–air mixtures, Proc. Combust. Inst. 37 (2019) 3627–3635.

[53] M. Zhao, J.-M. Li, C.J. Teo, B.C. Khoo, H. Zhang, Effects of variable total pressures on instability and extinction of rotating detonation combustion, flow, Turbul. Comb. 104 (2019) 261–290.

[54] X.P. Li, W.D. Liu, Y. Pan, L.C. Yang, B. An, Experimental investigation on laser-induced plasma ignition of hydrocarbon fuel in scramjet engine at takeover flight conditions, Acta Astronaut. 138 (2017) 79–84.

[55] V.R. Katta, K.Y. Cho, J.L. Hoke, J.R. Codoni, F.R. Schauer, W.M. Roquemore, Effect of increasing channel width on the structure of rotating detonation wave, Proc. Combust. Inst. 37 (2019) 3575–3583.

[56] J. Jodele, V. Anand, A. Zahn, N. Chiles, E. Gutmark, Quantification of rotating detonations using OH* chemiluminescence at varied widths, AIAA J. 59 (2021) 2457–2466.

[57] P. Wolanski, W. Balicki, W. Perkowski, A. Bilar, Experimental research of liquid-fueled continuously rotating detonation chamber, Shock Waves 6 (2021).

[58] V. Rodriguez, C. Jourdain, P. Vidal, R. Zitoun, An experimental evidence of steadily-rotating overdriven detonation, Combust. Flame 202 (2019) 132–142.

[59] R.W. Houim, R.T. Fievisohn, The influence of acoustic impedance on gaseous layered detonations bounded by an inert gas, Combust. Flame 179 (2017) 185–198.

[60] M. Short, C. Chiquete, J.J. Quirk, Propagation of a stable gaseous detonation in a circular arc configuration, Proc. Combust. Inst. 37 (2019) 3593–3600.

[61] X.M. Tang, J.P. Wang, Y.T. Shao, Three-dimensional numerical investigations of the rotating detonation engine with a hollow combustor, Combust. Flame 162 (2015) 997–1008.

[62] H.L. Zhang, W.D. Liu, S.J. Liu, Experimental investigations on H-2/air rotating detonation wave in the hollow chamber with Laval nozzle, Int. J. Hydrogen Energy 42 (2017) 3363–3370.

[63] H. Peng, W. Liu, S. Liu, H. Zhang, Experimental investigations on ethylene-air Continuous Rotating Detonation wave in the hollow chamber with Laval nozzle, Acta Astronaut. 151 (2018) 137–145.

[64] J. Braun, B.H. Saracoglu, G. Paniagua, Unsteady performance of rotating detonation engines with different exhaust nozzles, J. Propul. Power 33 (2017) 121–130.